Self-Assembly of Nanoclusters into Mono-, Few-, and Multilayered Sheets *via* Dipole-Induced Asymmetric van der Waals Attraction

Zhennan Wu,[†] Jiale Liu,[†] Yanchun Li,[‡] Ziyi Cheng,[†] Tingting Li,[†] Hao Zhang,[*,†] Zhongyuan Lu,[‡] and Bai Yang[†]

[†]State Key Laboratory of Supramolecular Structure and Materials, College of Chemistry, Jilin University, Changchun 130012, P. R. China and [‡]State Key Laboratory of Supramolecular Structure and Materials, Institute of Theoretical Chemistry, Jilin University, Changchun 130023, P. R. China

ABSTRACT Two-dimensional (2D) nanomaterials possessing regular layered structures and versatile chemical composition are highly expected in many applications. Despite the importance of van der Waals (vdW) attraction in constructing and maintaining layered structures, the origin of 2D anisotropy is not fully understood, yet. Here, we report the 2D self-assembly of ligand-capped Au_{15} nanoclusters into mono-, few-, and multilayered sheets in colloidal solution. Both the experimental results and computer simulation reveal that the 2D self-assembly is initiated by 1D dipolar attraction common in nanometer-sized objects. The dense 1D attachment of Au_{15} leads to a redistribution of the surface ligands, thus generating asymmetric vdW attraction. The deliberate control of the coordination of dipolar and vdW attraction further allows to manipulate the thickness and morphologies of 2D self-assembly architectures.

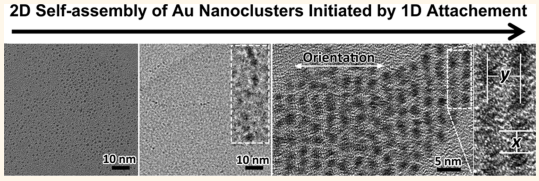

KEYWORDS: two-dimensional material · self-assembly · nanocluster · nanosheet · anisotropic vdW attraction

Two-dimensional (2D) nanomaterials whose atomic bonding along two-dimensions are similar but stronger than along the third dimension have attracted extraordinary attentions due to their unique layered structures and fascinating physical properties.[1−3] Wide investigations have revealed that the main attraction to hold the layers together is van der Waals (vdW) interaction, whereas the atoms or polyhedrals are connected by covalent, ionic, or other strong interactions within each layer.[4−6] This structural property permits to prepare mono-, few-, and multilayered 2D nanostructures with versatile chemical composition by careful selection of synthetic protocol, for example, top-down exfoliation and bottom-up synthesis.[7−11] Despite the importance in constructing and maintaining layered structures, vdW interaction is essentially isotropic.[12] The origin of anisotropy in the formation of layered architectures still deserves exhaustive studies.

As the key for synthesizing 2D nanomaterials in colloidal solution, the anisotropy can be generated by two pathways, namely formation of lamellar mesophase templates and 2D-orientated self-assembly of magic-size nanoclusters (NCs).[13−15] The template approaches are well understandable and applied to produce a variety of crystalline nanosheets,[9,11,16] whereas the self-assembly approaches are not fully understood, yet. Besides vdW interaction, 2D self-assembly also relates to other factors in NCs system, such as dipole moment, charge, hydrophobicity, and so forth.[12,17−19] The efforts on manipulating the cooperation and equilibrium of various interactions give the hope to perform NCs 2D self-assembly in controlled manner.[12]

It should be mentioned that self-assembly is the workhorse of current nanotechnology, which permits to achieve higher level architectures from preformed building blocks.[17] However, most efforts have been devoted to the 2D self-assembly of large building blocks, such as big nanoparticles,[20−22] polymers,[23] and proteins,[24] whereas limited successes are reported for ultrasmall NCs with diameter below 2 nm.[25,26] The limitation in producing 2D architectures through NCs self-assembly is mainly arisen from two reasons. As to ultrasmall NCs, their

* Address correspondence to hao_zhang@jlu.edu.cn.

Received for review March 26, 2015 and accepted June 1, 2015.

Published online June 01, 2015
10.1021/acsnano.5b01823

large surface energy makes them unstable during self-assembly. They prefer to recrystallize or fuse into big nanoparticles. In addition, for such small NCs, their interactions are rather weak, which is comparable to the thermal fluctuation energy of the surroundings.[27] The assembled NCs can be easily detached, thus restricting the formation of ordered structures. Consequently, exploring new methods for achieving NCs 2D self-assembly and in particular revealing the in-depth mechanism is highly important.

In this work, we investigate the self-assembly of ligand-capped Au_{15} NCs into mono-, few-, and multilayered sheets in colloidal solution, which is a typical model of polyhedral-thick 2D architectures. The permanent dipole of the NCs, resulting both from the specific arrangement of gold atoms and the surface distribution of capping ligands, generates the inter-NC dipolar attraction, and therewith initiates the 1D oriented self-assembly of NCs. This in return leads to the asymmetric distribution of ligands on NCs, thus generating anisotropic vdW attraction in the following 2D assembly. The acquirement of the origin of anisotropy makes it possible to further control the thickness, size, and morphologies of Au_{15}-based 2D architectures.

RESULTS AND DISCUSSION

The Au_{15} NCs (0.032 mmol) used to perform 2D self-assembly are foremost prepared in 2 mL benzyl ether (BE) at room temperature.[27] In this context, 1-dodecanethiol (DT, 2 mmol) acts as ligand *cum* reductant to react with Au (III), which produces the NCs composed of $Au(0)_{11}Au(I)_4DT_{15}$. The grafting density of DTs on NC surface is calculated as 1.9 per nm^2. Because of the molecule-like transition associated with the small diameter (1.5 ± 0.3 nm), the as-prepared Au_{15} NCs exhibit strong photoluminescence centered at 600 nm (Figures 1 and 2a).

In general, the formation of layered Au_{15} self-assembly architectures requires the annealing of Au_{15} BE solution over 140 °C. However, to monitor the structural evolution, important intermediates at different stages are captured and analyzed first (Figure 2b,c,e). As the solution is maintained at room temperature for 24 h, 1D-oriented self-assembly of Au_{15} NCs is observed (Figure 2b). After the solution is heated to 90 °C and maintained for 5 min, small isolated 2D architectures with width about 30 nm and length about 50 nm are found (Figure 2e). These isolated 2D architectures exhibit two different Au_{15} center-to-center distances about 2.2 and 3.6 nm in average, respectively, which is defined as "*x*" and "*y*" (Figure 2c). Small-angle X-ray powder diffraction (SAXD) clearly exhibits a peak at 2.44° corresponding to the *d* spacing of "*y*" = 3.6 nm, consisting with the regular arrangement of NCs along "$\vec{y}$" direction (Figure 3). Despite the distinct peak at 3.65° corresponding

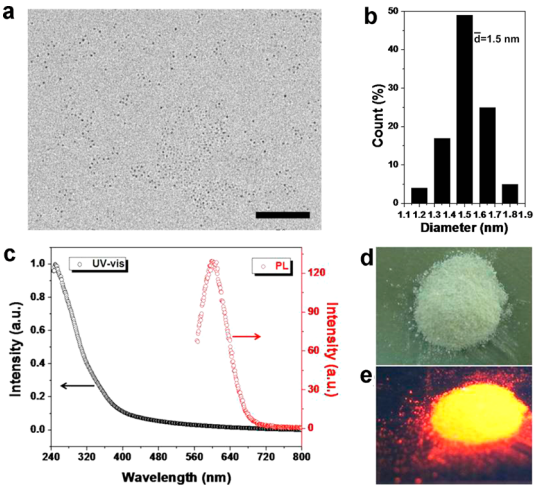

Figure 1. TEM image (a) and the size distribution (b) of Au_{15} NCs foremost prepared in BE solution at room temperature. The corresponding UV−vis absorption and PL emission spectra excited by 320 nm ultraviolet light are shown in (c). Optical (d) and PL (e) images of the powder of Au_{15} NCs. The scale bar is 50 nm in (a).

to "*x*" = 2.2 nm is not observed, the characteristic region from 3.5° to 3.8° is much broad. This reveals the heterogeneity of NCs along "$\vec{x}$" direction, which is confirmed by the transmission electron microscopy (TEM) observation (Figure 2c).

The anisotropy of NC spatial arrangement is attributed to the different driving forces as NCs assemble along "$\vec{x}$" and "$\vec{y}$" directions. As to Au_{15} NCs dispersed in nonpolar solvents, the inter-NC interactions mainly involve dipole−dipole and vdW attractions. Dipolar attraction is anisotropic, and vdW attraction is isotropic. In addition, dipolar attraction is impactful in longer distance ($\sim 1/r^3$) than vdW attraction ($\sim 1/r^6$).[28] So, like the self-assembly of most nanometer-sized particles and clusters,[18] 1D orientation of Au_{15} NCs is triggered by dipole−dipole attraction in the initial stage (Figure 2b). By considering the specific arrangement of intrinsic Au atoms and the distribution of DTs on Au_{15} (Figure 4), computer aided calculation indicates that the permanent dipole moment (μ) of $Au_{15}DT_{15}$ is 13.27 D.[29] The energy of dipolar attraction between two NCs is calculated according to the classical formula for aligned dipoles $E = -\mu^2/2\pi\varepsilon_0 r\,(r^2 - d_{NC}^2)$,[18] where ε_0 is 8.85×10^{-12} C^2 J^{-1} m^{-1}. By further estimating the center-to-center interdipolar separation *r* as 2.2 nm for the NCs with diameter d_{NC} of 1.5 nm, the energy afforded by 13.27 D is 3.8 kJ/mol, which is higher both than the energy of regular molecular dipole−dipole attraction (1.5 kJ/mol) and the molar kinetic energy at 25 °C (2.4 kJ/mol).[18] This means that the dipolar attraction between Au_{15} NCs is strong enough to drive 1D self-assembly, thus leading to the spatial distance of "*x*". Even at 90 °C, the permanent dipole is still higher than the corresponding molar kinetic energy (2.9 kJ/mol). So, the distance of "*x*" is maintained (Figure 2c).

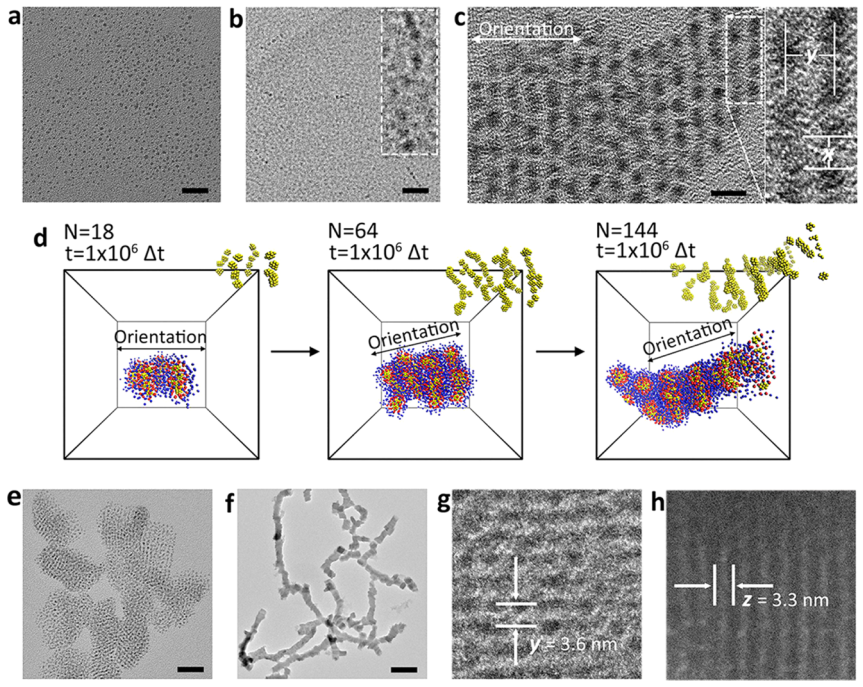

Figure 2. Temperature-dependent morphology evolution of Au_{15} self-assembly architectures in BE. (a–c) TEM images of the Au_{15} NCs after incubating at 25 °C for 1 h (a) and 24 h (b), and at 90 °C for 5 min (c). (d) Computer simulation results of dipole-induced linear arrangement of Au_{15} NCs and the subsequent aggregation with increasing the concentration from N = 18 to 144 at the BD time unit t = 1 000 000 Δt. (e) TEM image of the small isolated 2D architectures, which is the low magnification counterpart of (c). (f–h) TEM images of the Au_{15} architectures that are incubated at 140 °C for 5 min. (f and g) The top view with low (f) and high (g) magnification. (h) The side view of the architectures. The scale bar is 10 (a), 10 (b), 5 (c), 20 (e), and 300 nm (f).

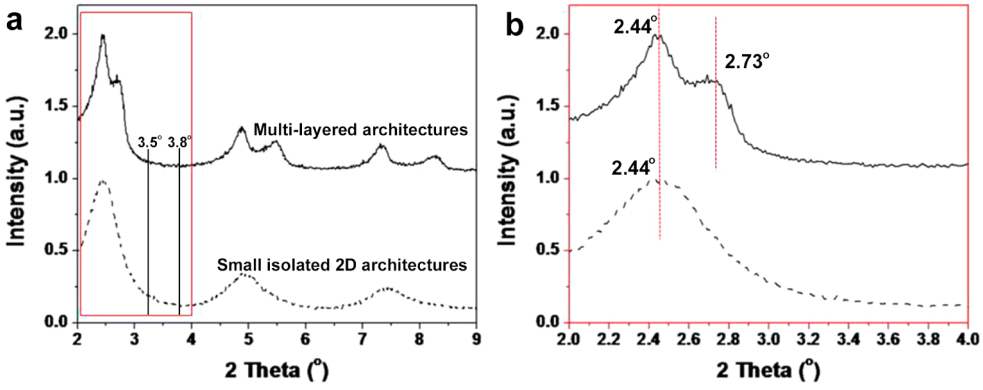

Figure 3. SAXD spectra of small isolated 2D architectures with elongated feature and multilayered 2D architectures, which are incubated at 90 and 140 °C for 5 min, respectively.

Note that the surface-to-surface distance of Au_{15} NCs along "$\vec{x}$" direction is only 0.7 nm, which is even shorter than the length of one DT chain in elongated feature that should be 1.7 nm.[27] It implies that the steric repulsion of neighboring Au_{15} NCs along "$\vec{x}$" direction is capable to drive DTs orientating vertical to "$\vec{x}$" direction (Figure 5a). Brownian dynamics (BD) is performed to simulate the anisotropy in Au_{15} NC arrangement by considering the specific structure of $Au_{15}DT_{15}$ (Supporting Information Figure S1).[17] The result indicates when several Au_{15} NCs attach to each other, DTs can accommodate new configuration and redistribute on NC surface. This mainly attributes to the variation of Au–S bond length during the self-assembly (Supporting Information Figure S1c). Meaningfully, the simulation further indicates that the distribution of DTs is more preferential along "$\vec{y}$" direction than another "$\vec{z}$" direction vertical to "$\vec{x}$", though DTs are rich both along "$\vec{y}$" and "$\vec{z}$" directions. Accordingly, the grafting density of DTs on NC surface alters to 0.8 per nm^2 along "$\vec{x}$" direction and 2.2 per nm^2 along "$\vec{y}$" direction (Supporting Information Figure S2). As a result, an asymmetric vdW attraction is induced. In this case, the surface-to-surface distance of Au_{15} NCs along "$\vec{y}$" direction is 2.1 nm, which is between the length of one DT and two DTs. This implies the formation of

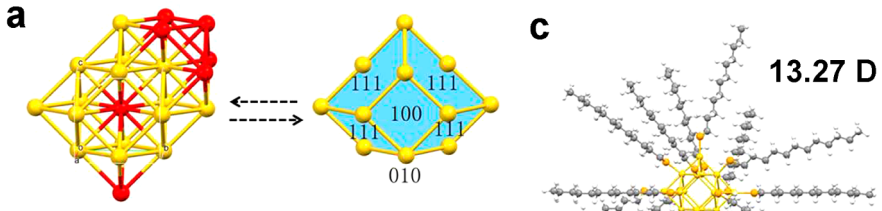

b

Symmetry	C_{2v}	
Energy Values (eV)	PBE / DNP level of theory	0.00
	PBEPBE / LANL2DZ level of theory	0.04
	PBEPBE / SDD+Au (2f) // PBEPBE / LANL2DZ level of theory	0.00

Figure 4. Relative stability of Au_{15} arrangement from the bulk-crystal structures of gold (a) that presents C_{2v} symmetry and lowest-energy. The energy values based on the PBE/DNP level, the PBEPBE/LANL2DZ level, and the PBEPBE/SDD+Au 2f// PBEPBE/LANL2DZ level of theory is 0.00, 0.04, and 0.00 eV, respectively (b). $Au_{15}DT_{15}$ NC is sketched by GaussView 5.0.8 and optimized by the VAMP module. On the basis of the simulative construction of $Au_{15}DT_{15}$ NC (c), the dipole moment of $Au_{15}DT_{15}$ NC is calculated as 13.27 D.

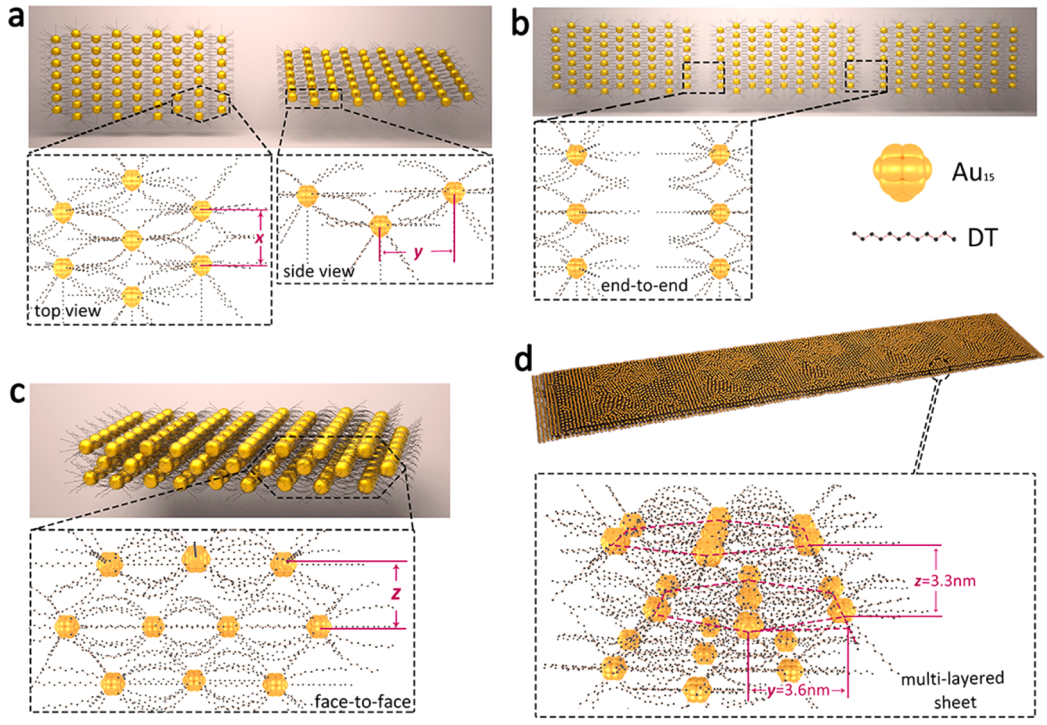

Figure 5. Schematic illustration of the morphology variation from small isolated 2D architectures to multilayered architectures under heating treatment at 140 °C. (a–d) The cartoon pictures describe the secondary assembly of small isolated architectures into long multilayered architectures, which involve the distribution of DT alkyls over elongated architectures (a), the end-to-end (b) and face-to-face self-assembly (c), and the spatial arrangement of Au_{15} NCs within the multilayered architectures (d).

overlapping structure of the DTs on neighboring Au NCs along "$\vec{y}$" direction, thus providing strong vdW interaction.[30] The vdW attraction of DTs between the neighboring Au_{15} NCs is calculated more than 7 k_BT, where k_B is the Boltzmann constant and T is the absolute temperature.[27] In addition, the BD simulation agrees well with the experimental results. Namely, at the BD time unit $t = 1 \times 10^6\ \Delta t$, the self-assembly of Au_{15} NCs follows the initial linear arrangement induced by dipolar attraction along "$\vec{x}$" direction, and subsequently along "$\vec{y}$" direction. BD simulation also reveals that the 2D-oriented self-assembly is more competitive than 1D with increasing concentration of Au_{15} NCs from $N = 18$ to 144 (Figure 2d), because vdW attraction depends more greatly on the inter-NC distance than dipolar attraction.[28]

Despite the formation of small isolated 2D architectures at 90 °C, such structures are unstable in the solution due to the high energy along "$\vec{y}$" and subsequent "$\vec{z}$" direction. To obtain stable structures, the

Au_{15} BE solution must be heated to 140 °C that allows for the growth in length, width, and thickness, which produces long multilayered 2D architectures (Figure 2f–h). TEM and AFM observations reveal that the 2D architectures possess the thickness of 100 ± 20 nm, width of 150 ± 20 nm, and the length of 500–2000 nm (Figure 2f and Supporting Information Figure S3). These 2D architectures are composed of multiple domains, because they are the secondary assemblies from the small 2D architectures shown in Figure 2e. This also means that the size and shape of domains should relate to those of initial small 2D architectures, which can be looked as the nucleus. Moreover, the intermediates of such secondary assembly are captured at 120 and 130 °C and revealed by TEM, which clearly show the attachment and coalescence of small 2D architectures (Supporting Information Figure S4). In this process, the attachment of small 2D architectures exhibits both end-to-end and face-to-face features (Figure 5b,c), because DTs, which contribute to the vdW attraction, are rich both in the ends and the faces of the initial small 2D architectures. The end-to-end assembly contributes to the length, while the face-to-face assembly contributes to the thickness of the layer structure. Vague binding boundary is observed along the longitudinal direction of the architectures, indicating the end-to-end assembly possesses defects (Figure 2f).

The distribution and interaction of DT alkyl chains are schemed in Figure 5, which clearly illustrate the morphology evolution of Au_{15} self-assembly architectures. In this context, individual Au_{15} NCs capped by DTs are driven by anisotropic dipolar attraction to trigger 1D-oriented arrangement along "$\vec{x}$" direction, and therewith repulse the surface DT distribution preferentially along "$\vec{y}$" direction (Figure 5a). As a result, an asymmetric vdW attraction is generated. We do not exclude the generation of vdW interaction from Au cores. But this interaction is isotropic and much weaker than that between DTs, thus can be neglected in 2D self-assembly.[28] Moreover, heating treatment makes DT more dynamic that allows further 2D-oriented assembly along "$\vec{y}$" direction. This process can be looked as the nucleation stage of Au_{15} self-assembly architectures.[27,31] With respect to the density of remaining DTs on the 2D nucleus, DTs preferentially distribute on the two ends along "$\vec{y}$" direction and subsequently on the two faces (Figure 5a). Consequently, in the following growth stage, the attachment and coalescence of the nucleus exhibit the priority in end-to-end and subsequent face-to-face features (Figure 5b,c). The end-to-end assembly keeps along "$\vec{y}$" direction, while the face-to-face assembly is along "$\vec{z}$" direction that vertical to both "$\vec{x}$" and "$\vec{y}$" directions. In the final multilayered 2D architectures, a new Au_{15} center-to-center distance of 3.3 nm is found (Figure 2h). By combining TEM and SAXD results, this distance is assigned as interlayer distance of "z" (Figures 2h and 3). SAXD results show that the primary distance "x" = 2.2 nm disappears in the final multilayered 2D architectures, indicating the redistribution of Au_{15} NCs during heating treatment at 140 °C (Figure 5d). In this context, the stability of dipole chains is temperature-dependent. At 140 °C, the molar kinetic energy of dipole chains is 3.3 kJ/mol, which is comparable with the energy of permanent dipole (3.8 kJ/mol). The relative weak dipolar force can no longer maintain the structures with 1D feature in the presence of enhanced vdW interaction. The two Au_{15}–Au_{15} distances of "y" and "z" in the multilayered architectures mean that the existence of two kinds of vdW interactions, namely, stronger inner-layer interaction and weaker inter-layer interaction are in accord with the structural property of vdW materials.[1–6]

To produce monolayered self-assembly architectures, the inter-NC interactions should be finely tuned to break the interlayer interaction without destroying the inner-layer one. Inspired by the liquid exfoliation strategy for preparing defect-free graphene,[7,8] the surface tension of solvent is considered to neutralize the interlayer vdW attraction of Au_{15} self-assembly architectures. The surface tension and vdW attraction should be very close. The energy balance can be expressed as the enthalpy of mixing, ΔH_{Mix}, which is calculated according to $\Delta H_{Mix}/V_{Mix} \approx (2/T)(\delta_{Au} - \delta_{sol})^2\phi$.[7,8] Where $\delta_i = \sqrt{E^i_{Sur}}$ is the square root of the component surface energy. T and ϕ is the thickness of Au_{15} self-assembly architectures, and the volume fraction, respectively. It shows that ΔH_{Mix} depends on the balance of Au_{15} vdW surface energy (δ_{Au}) and solvent surface energy (δ_{sol}). δ_{Au} is defined as the energy per unit area required to overcome the vdW forces as peeling two sheets apart. The vdW surface energy belonging to inter-layer and inner-layer is calculated to be 15.6 and 23.4 mJ/m^2, respectively (Supporting Information, Figure S5). In this respect, BE is not a suitable solvent to produce monolayered architectures, because of the high surface tension of 27.7 mJ/m^2 at 140 °C.[32] To lower the surface tension to 15.6 mJ/m^2, the temperature must exceed 250 °C (Supporting Information, Figure S6). However, such high temperature results in excessive conformational entropy of DT alkyls, which will destroy the inner-layered interaction and leads to random aggregates (Supporting Information Figure S7). To solve this problem, liquid paraffin (LP) with a surface tension of 15.4 mJ/m^2 at 140 °C is added to lower the surface tension of BE (Supporting Information, Figure S6).[32] As shown in Figure 6b-iii, monolayered Au_{15} self-assembly architectures are obtained as annealing at 140 °C for 60 min in the binary solvents of BE and LP with the volume ratio of 1/7.5. The temporal evolution of the self-assembly architectures from multi-, few-, to

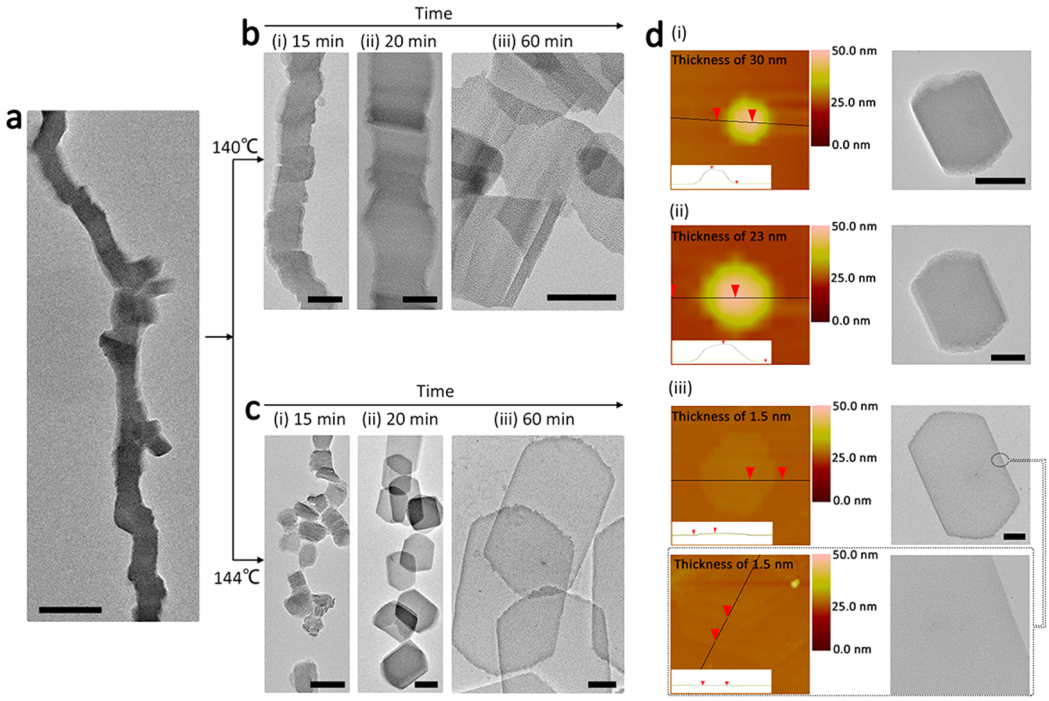

Figure 6. Time-dependent morphology evolution of Au_{15} self-assembly architectures at 140 and 144 °C for 60 min after adding LP. (a) TEM image of the as-prepared multilayered architectures. (b) Typical TEM images of the architectures as maintaining the multilayers at 140 °C for 15 (b-i), 20 (b-ii), and 60 (b-iii) min. (c) Typical TEM images of the architectures as maintaining the multilayers at 144 °C for 15 (c-i), 20 (c-ii), and 60 (c-iii) min. (d) Tapping modal AFM and corresponding TEM images of hexagonal nanosheets, which form at 144 °C for 15 (d-i), 20 (d-ii), and 60 (d-iii) min. The scale bar is 200 nm.

monolayer in BE and LP mixture is revealed by TEM observation (Figure 6a,b). As extending the annealing duration from 0, 15, 20, to 60 min, the width of the architectures increases from 100, 200, 400, to 600 nm. Accordingly, the thickness decreases from 100, 60, 30, to 1.5 nm (Supporting Information Figures S3 and S8). Meanwhile, the long architectures divide into separate Au_{15} monolayer. Such reorganization involves three aspects. First, the annealing at 140 °C activates the mobility of DTs in the multilayered 2D architectures,[33−36] thus permitting the sliding reorganization of Au_{15} NCs. Second, the surface tension is lowered in BE and LP mixture, which decreases the thickness of 2D architectures like liquid exfoliation. Finally, because the multilayered architectures are the aggregates of smaller 2D architectures (Figure 2f and Supporting Information Figure S4), the connection at specific regions, such as the interdomains, is weaker. Therefore, the disassembly of long architectures is allowed during the structural reorganization. Note that the monolayered sheets are stable, which preserve the morphology after maintaining at 140 °C for 5 h (Supporting Information Figure S9). Large nanoparticles are observed only at higher temperature, such as at 250 °C for 3 h (Supporting Information Figure S10).

To confirm the consideration, the multilayered 2D architectures are annealed at 144 °C. Such variation produces hexagonal nanosheets with controllable thickness (Figure 6c,d). In this context, the elevated temperature lowers the surface tension of solvents but increases the conformational entropy of DTs,[27,31] thus facilitating the sliding reorganization of Au_{15} NCs and the disassembly of long architectures at the poorly connected points. Separate assembles with ellipsoid feature are observed after 15 min annealing (Figure 6c-i). Owing to the stretch stemming from the adjacent NCs, the boundary of ellipsoids is straightened during further annealing.[37] As a result, hexagonal individuals of self-assembly architectures are produced (Figure 6c-ii and iii). Similar to the structural evolution at 140 °C, a prolonged annealing at 144 °C increases the size but decreases the thickness of hexagonal nanosheets. The sliding reorganization of Au_{15} also exists, which is parallel to the sheets but orients randomly (Supporting Information Figure S11). AFM results exhibit a gradual thickness decrease to 30, 23, and 1.5 nm (Figure 6d). Note that 1.5 nm is the diameter of individual Au_{15} NCs, showing the monolayer feature. Despite the fact that both disassembly and sliding reorganization are important for producing monolayered sheets, the dominance depends on the different stages of self-assembly. At the initial stage, the disassembly is dominant because of the poorly connected Au NCs in long architectures. So, separate assemblies with ellipsoid feature are produced (Figure 6c-i). At the following annealing treatment, sliding

reorganization becomes dominant, because the attraction between Au NCs is much stronger through the overlapping of DT alkyls.

In all, the formation of monolayered sheets is mainly attributed to the secondary solution of LP and the strong overlapping of DTs. LP lowers the surface tension of solvent to neutralize the interlayer vdW attraction, and therewith facilitates the formation of monolayered sheets. As replacing LP by other low surface tension solvents, such as octadecene, monolayered sheets are also produced (Supporting Information Figure S12). The DTs on neighboring NCs are strongly overlapped, which allows the sliding reorganization rather than fusion of NCs. As shown in Supporting Information Figure S13a, similar monolayered sheets are produced using hexadecanethiol as the ligand, which possesses longer alkyls than DT, whereas big nanoparticles form using pentanethiol with shorter length as the ligand (Supporting Information Figure S13b).

By understanding the origin of asymmetric driving force and entropic effect in forming 2D-oriented Au_{15} self-assembly architectures, the morphologies of architectures are further controlled (Figure 7). For example, nanoleaves are obtained by decreasing the concentration of Au_{15} NCs (0.008 mmol) and annealing at 142 °C (Figure 7b). Such variation mainly influences the balance of dipolar and vdW interactions in the formation of initial 2D nucleus. In this context, the permanent dipole of Au_{15} NCs is independent of the concentration. NCs concentration only affects the relative intensity of vdW interaction and dipolar forces, because higher concentration generates stronger vdW interaction by shortening the distance of NCs. As simulated in Figure 1d, low Au_{15} concentration suppresses the nucleation in 2D feature, thus generating narrow adjacent domains in the intermediate structures. These domains adhere through the long side, which is the "$\vec{y}$" direction (Supporting Information Figure S14). So, after disassembly, narrow self-assembly architectures are obtained. Moreover, the aspect ratio of hexagonal nanosheets is tuned from 1.6 to 4.9 by increasing the heating rate (Figure 7c,d). The increased heating rate means the shortened duration to reach a specific temperature, such as 144 °C for the growth of nanosheets. The shortened annealing duration leads to insufficient sliding organization of Au_{15} in each domain toward "$\vec{y}$" direction, which is also the direction of domain adhesion (Supporting Information Figure S15). As a result, high aspect ratio hexagonal sheets are produced after disassembly.

It should be mentioned that the current approach cannot be extended to the 2D self-assembly of big nanoparticles, owing to the difference in the driving forces like ultrasmall NCs. In our approach, the 2D self-assembly is mainly driven by the asymmetric vdW

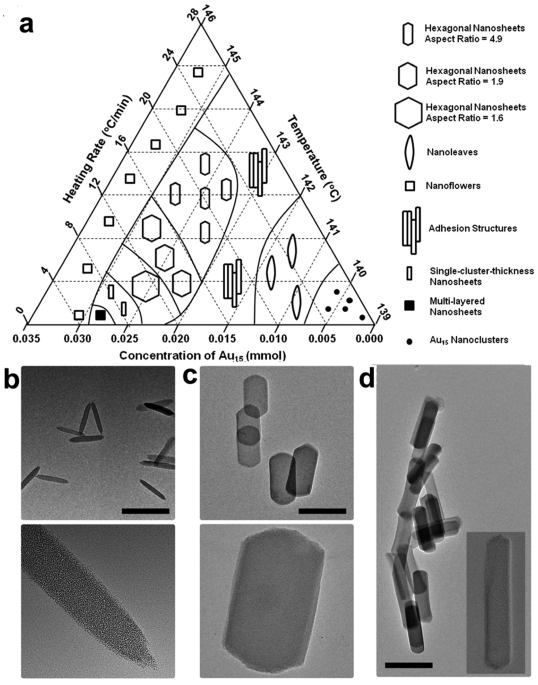

Figure 7. A variety of Au_{15} self-assembly architectures. (a) Product diagram of the architectures by altering the concentration of Au_{15}, reaction temperature, and heating ratio. (b–d) Typical TEM images of the architectures with well-defined morphology, for example, nanoleaves (b), and more lanky hexagonal nanosheets with the aspect ratio of 1.9 (c) and 4.9 (d). The scale bar is 200 nm.

interaction, resulting from the asymmetric distribution of capping ligands on NCs. Whereas the vdW interaction from the core of Au NCs is negligible for their small size, for big nanoparticles, the vdW interaction from the core of particles is much stronger than that from capping ligands.[28] Thus, the ligands distribution cannot induce enough asymmetry for 2D self-assembly.

CONCLUSIONS

In conclusion, mono-, few-, and multilayered 2D architectures with controlled morphologies are produced through the self-assembly of $Au_{15}DT_{15}$ NCs in colloidal solution. The main driving forces of such self-assembly are the dipolar interaction originated from the specific structure of NCs and the vdW interaction contributed from DTs. Triggered by the anisotropic dipolar attraction, the initial assembly is 1D-oriented, which in return leads to the asymmetric spatial distribution of DTs and hence the vdW attraction. As a result, the followed self-assembly is conducted toward 2D model. With respect to control 2D morphologies, the entropic effect is important for the reorganization of NCs in the preassembled structures. This acquirement permits to tune the length, aspect ratio, and thickness of the final 2D architectures. The current work presents a facile and feasible approach to produce NC-based 2D self-assembly structures in colloidal solution. In particular, the in-depth understanding of

the origin and control of asymmetric vdW attraction in 2D self-assembly offers a new pathway for designing practical vdW materials with broadened compositions and morphologies.

METHODS

Materials. 1-Dodecanethiol (DT, 98%) was purchased from Aladdin Chemistry Co. Ltd. Benzyl ether (BE, 98%) was purchased from Aldrich. Chloroauric acid ($HAuCl_4 \cdot 4H_2O$, Au mol % >47.8%) and liquid paraffin (LP, CP) were purchased from the Sinopharm Chemical Reagent Co. Ltd. Acetone and chloroform were all commercially available products and used as received without further purification.

Preparation of Au_{15} NCs. A total of 0.2 g (0.032 mmol) of $HAuCl_4 \cdot 4H_2O$ was dissolved by 2 mL of BE in a 100 mL three-necked flask. Under vigorous stirring, 0.5 mL of DT (2 mmol) was added dropwise at room temperature and maintained for 1 h to produce Au_{15} NCs.

1D-Oriented Self-Assembly of Au_{15} NCs. To conduct 1D-oriented self-assembly, the Au_{15} BE solution was maintained at room temperature for 24 h after removal of the excessive DT using chloroform.

Self-Assembly of Au_{15} NCs into Multilayered Architectures. The aforementioned Au_{15} BE solution was heated from room temperature to 140 °C at the rate of 5 °C/min under vacuum and vigorous stirring. When the temperature was up to 140 °C, multilayered architectures were produced.

Self-Assembly of Au_{15} NCs into Monolayered Architectures. The preparation of monolayered architectures was similar to that of multilayered architectures, except for adding 15 mL of LP into BE solution as a secondary solvent (7.5:1 LP-to-BE volume ratio).

Self-Assembly of Au_{15} NCs into Separate Architectures with Well-Defined Morphologies. For a typical preparation of well-defined hexagonal nanosheets with the aspect ratio of 1.6, the foremost synthesized Au_{15} NCs were maintained for 60 min at 144 °C in binary solvent of 15 mL LP and 2 mL BE (7.5:1 LP-to-BE volume ratio), and under N_2 protection after degassing under vacuum. The heating rate was 10 °C/min. To produce well-defined hexagonal nanosheets with the aspect ratio of 1.9 and 4.9, similar operation was adopted except using the heating rate of 13 and 20 °C/min, respectively.

To produce well-defined nanoleaves, first, 0.05 g of $HAuCl_4 \cdot 4H_2O$ was dissolved by 2 mL BE in a 100 mL three-necked flask. Under vigorous stirring, 0.125 mL of DT was added dropwise at room temperature and maintained for 1 h to produce Au_{15} NCs (0.008 mmol Au_{15}). Subsequently, 30 mL of LP was added as a secondary solvent (15:1 LP-to-BE volume ratio). The mixture was maintained for 10 min at 142 °C and under N_2 protection after degassing under vacuum. The heating rate was 10 °C/min.

To produce well-defined nanoflowers, the preparation was similar to that of hexagonal nanosheets with the aspect ratio of 1.6, except elevating the temperature over 145 °C.

To produce adhesion structures, the preparation was similar to that of hexagonal nanosheets with the aspect ratio of 1.6, except lowering the concentration of Au_{15} to 0.015 mmol.

Purification. After it was cooled down to room temperature, 1 mL solution of Au_{15} self-assembly architectures was washed and precipitated through the addition of 1 mL of chloroform and 2 mL of acetone twice at room temperature. Separated by centrifugation, the precipitates were collected and dispersed in 1 mL of chloroform.

Characterization. UV−visible absorption spectra were measured by a Shimadzu 3600 UV−vis-NIR spectrophotometer. Fluorescence spectroscopy was measured using a Shimadzu RF-5301 PC spectrophotometer. Transmission electron microscopy (TEM) was measured with a Hitachi H-800 electron microscope, which was at an acceleration voltage of 200 kV with a CCD camera. High-resolution TEM (HRTEM) images were acquired with a JEM-2100F electron microscope at 200 kV. Atomic force microscope (AFM) tapping mode measurements were performed on a Nanoscope IIIa scanning probe microscope (Digital Instruments) and by a rotated tapping mode etched silicon probe tip. Small-angle X-ray powder diffraction (SAXD) investigation was carried out on a Rigaku X-ray diffractometer using Cu K radiation (λ = 1.5418 Å).

Model and Simulation Method. Material Studio version 5.0, a high-quality quantum mechanics computer program was used to calculate the quantum chemical parameters of $Au_{15}DT_{15}$ NCs. These calculations employed AM1 semiempirical equations at RHF level implemented in the VAMP module. First, the Au_{15} NC was generated from crystal structure,[38] which agreed with the relative stability of neutral Au_{15} NCs as shown in Figure 4a,b.[39] Then, $Au_{15}DT_{15}$ NC was sketched by GaussView 5.0.8 and optimized by the VAMP module as shown in Figure 4c. Finally, we obtained the dipole moment as 13.27 D and the charge distribution of Au in $Au_{15}DT_{15}$.

We adopted 15 linear chains connected to a center Au core to form the composite system $Au_{15}DT_{15}$, where Au_{15} represented 15 CG beads form a spherical rigid body. Brownian dynamics (BD) simulation technique, a suitable and efficient method in treating the self-assembly of nano-objects, was used to simulate the stepwise interaction between $Au_{15}DT_{15}$ NCs in BE solution (Supporting Information Figure S1).

Conflict of Interest: The authors declare no competing financial interest.

Supporting Information Available: Additional simulation, calculation, schematic illustration, AFM images, and TEM images of NCs 2D self-assembly. The Supporting Information is available free of charge on the ACS Publications website at DOI: 10.1021/acsnano.5b01823.

Acknowledgment. This work was supported by the 973 Program of China (2014CB643503), NSFC (51425303, 21374042, 21174051, 91123031, 51433003, 21221063, 51403022), Natural Science Foundation of Jilin Province (20140101048JC), and the Special Project from MOST of China. H.Z. proposed and supervised the project. H.Z., Z.N.W., and B.Y. designed and performed the experiments and co-wrote the paper. J.L.L., Z.Y.C. and T.T.L. participated in most experiments. Z.Y.L. and Y.C.L designed and performed the computer simulations.

REFERENCES AND NOTES

1. Chhowalla, M.; Shin, H. S.; Eda, G.; Li, L.; Loh, K. P.; Zhang, H. The Chemistry of Two-Dimensional Layered Transition Metal Dichalcogenide Nanosheets. *Nat. Chem.* **2013**, *5*, 263–275.
2. Yu, J. H.; Liu, X.; Kweon, K. E.; Joo, J.; Park, J.; Ko, K.; Lee, D. W.; Shen, S.; Tivakornsasithorn, K.; Son, J. S.; et al. Giant Zeeman Splitting in Nucleation-Controlled Doped CdSe: Mn^{2+} Quantum Nanoribbons. *Nat. Mater.* **2010**, *9*, 47–53.
3. Ithurria, S.; Tessier, M. D.; Mahler, B.; Lobo, R. P. S. M.; Dubertret, B.; Efros, A. L. A. L. Colloidal Nanoplatelets with Two-Dimensional Electronic Structure. *Nat. Mater.* **2011**, *10*, 936–941.
4. Zhang, X.; Xie, Y. Recent Advances in Free-Standing Two-Dimensional Crystals with Atomic Thickness: Design, Assembly and Transfer Strategies. *Chem. Soc. Rev.* **2013**, *42*, 8187–8199.
5. Butler, S. Z.; Hollen, S. M.; Cao, L.; Cui, Y.; Gupta, J. A.; Gutiérrez, H. R.; Heinz, T. F.; Hong, S. S.; Huang, J.; Ismach, A. F.; et al. Progress, Challenges, and Opportunities in Two-Dimensional Materials Beyond Graphene. *ACS Nano* **2013**, *7*, 2898–2926.
6. Dubertret, B.; Heine, T.; Terrones, M. The Rise of Two-Dimensional Materials. *Acc. Chem. Res.* **2015**, *48*, 1–2.
7. Hernandez, Y.; Nicolosi, V.; Lotya, M.; Blighe, F. M.; Sun, Z.; De, S.; McGovern, I. T.; Holland, B.; Byrne, M.; Guńko, Y.; et al. High-Yield Production of Graphene by

Liquid-Phase Exfoliation of Graphite. *Nat. Nanotechnol.* **2008**, *3*, 563–568.
8. Coleman, J. N.; Lotya, M.; O'Neill, A.; Bergin, S. D.; King, P. J.; Khan, U.; Young, K.; Gaucher, A.; De, S.; Smith, R. J.; et al. Two-Dimensional Nano-Sheets Produced by Liquid Exfoliation of Layered Materials. *Science* **2011**, *331*, 568–571.
9. Bouet, C.; Tessier, M. D.; Ithurria, S.; Mahler, B.; Nadal, B.; Dubertret, B. Flat Colloidal Semiconductor Nanoplateles. *Chem. Mater.* **2013**, *25*, 1262–1271.
10. Joo, J.; Son, J. S.; Kwon, S. G.; Yu, J. H.; Hyeon, T. Low-Temperature Solution-Phase Synthesis of Quantum Well Structured CdSe Nanoribbons. *J. Am. Chem. Soc.* **2006**, *128*, 5632–5633.
11. Huang, X.; Li, S.; Huang, Y.; Wu, S.; Zhou, X.; Li, S.; Gan, C. L.; Boey, F.; Mirkin, C. A.; Zhang, H. Synthesis of Hexagonal Close-Packed Gold Nanostructures. *Nat. Commun.* **2011**, *2*, 292.
12. Tang, Z.; Zhang, Z. L.; Wang, Y.; Glotzer, S. C.; Kotov, N. A. Self-Assembly of CdTe Nanocrystals into Free-Floating Sheets. *Science* **2006**, *314*, 274–278.
13. Liu, Y.; Wang, F.; Wang, Y.; Gibbons, P. C.; Buhro, W. E. Lamellar Assembly of Cadmium Selenide Nanoclusters into Quantum Belts. *J. Am. Chem. Soc.* **2011**, *133*, 17005–17013.
14. Wang, Y.; Liu, Y.; Zhang, Y.; Wang, F.; Kowalski, P. J.; Rohrs, H. W.; Loomis, R. A.; Gross, M. L.; Buhro, W. E. Isolation of the Magic-Size CdSe Nanoclusters $[(CdSe)_{13}(n\text{-octylamine})_{13}]$ and $[(CdSe)_{13}(\text{oleylamine})_{13}]$. *Angew. Chem., Int. Ed.* **2012**, *51*, 6154–6157.
15. Son, J. S.; Wen, X.; Joo, J.; Chae, J.; Baek, S.; Park, K.; Kim, J. H.; An, K.; Yu, J. H.; Kwon, S. G.; et al. Large-Scale Soft Colloidal Template Synthesis of 1.4 nm Thick CdSe Nanosheets. *Angew. Chem., Int. Ed.* **2009**, *48*, 6861–6864.
16. Yang, J.; Son, J. S.; Yu, J. H.; Joo, J.; Hyeon, T. Advances in The Colloidal Synthesis of Two-Dimensional Semiconductor Nanoribbons. *Chem. Mater.* **2013**, *25*, 1190–1198.
17. Xia, Y.; Nguyen, T. D.; Yang, M.; Lee, B.; Santos, A.; Podsiadlo, P.; Tang, Z.; Glotzer, S. C.; Kotov, N. A. Self-Assembly of Self-Limiting Monodisperse Supraparticles from Polydisperse Nanoparticles. *Nat. Nanotechnol.* **2011**, *6*, 580–587.
18. Tang, Z.; Kotov, N. A.; Giersig, M. Spontaneous Organization of Single CdTe Nanoparticles into Luminescent Nanowires. *Science* **2002**, *297*, 237–240.
19. Tang, Z.; Kotov, N. A. One-Dimensional Assemblies of Nanoparticles: Preparation, Properties, and Promise. *Adv. Mater.* **2005**, *17*, 951–962.
20. Cheng, W.; Campolongo, M. J.; Cha, J. J.; Tan, S. J.; Umbach, C. C.; Muller, D. A.; Luo, D. Free-Standing Nanoparticle Superlattice Sheets Controlled by DNA. *Nat. Mater.* **2009**, *8*, 519–525.
21. Ng, C. K.; Udagedara, I. B.; Rukhlenko, I. D.; Chen, Y.; Tang, Y.; Premaratne, M.; Cheng, W. Free-Standing Plasmonic-Nanorod Superlattice Sheets. *ACS Nano* **2012**, *6*, 925–934.
22. Si, K. J.; Sikdar, D.; Chen, Y.; Eftekhari, F.; Xu, Z.; Tang, Y.; Xiong, W.; Guo, P.; Zhang, S.; Lu, Y.; et al. Giant Plasmene Nanosheets, Nanoribbons, and Origami. *ACS Nano* **2014**, *8*, 11086–11093.
23. Niu, T.; Gu, Y.; Huang, J. Luminescent Cellulose Sheet Fabricated by Facile Self-Assembly of Cadmium Selenide Nanoparticles on Cellulose Nanofibres. *J. Mater. Chem.* **2011**, *21*, 651–656.
24. Gu, Y.; Huang, J. Reversible Self-Assembly of Ferritin Molecules for Fabrication of Size Controlled Microspheres and Microrods. *New J. Chem.* **2013**, *37*, 2624–2627.
25. Li, L.; Wang, Q. Spontaneous Self-Assembly of Silver Nanoparticles into Lamellar Structured Silver Nanoleaves. *ACS Nano* **2013**, *7*, 3053–3060.
26. Wang, F.; Zhang, X.; Zhang, Z.; He, C. *In Situ* Formation and Ordered Assembly of Gold Nanoclusters to Nano-Ribbonsat the Oil/Water Interface. *J. Mater. Chem.* **2011**, *21*, 15167–15170.
27. Wu, Z. N.; Dong, C.; Li, Y.; Hao, H.; Zhang, H.; Lu, Z.; Yang, B. Self-Assembly of Au_{15} into Single-Cluster-Thick Sheets at the Interface of Two Miscible High-Boiling Solvents. *Angew. Chem., Int. Ed.* **2013**, *52*, 9952–9955.
28. Bishop, K. J. M.; Wilmer, C. E.; Soh, S.; Grzybowski, B. A. Nanoscale Forces and Their Uses in Self-Assembly. *Small* **2009**, *5*, 1600–1630.
29. Bulusu, S.; Zeng, X. C. Structures and Relative Stability of Neutral Gold Clusters: Au_n (n = 15−19). *J. Chem. Phys.* **2006**, *125*, 154303.
30. Fan, H.; Yang, K.; Boye, D. M.; Sigmon, T.; Malloy, K. J.; Xu, H.; López, G. P.; Brinker, C. J. Self-Assembly of Ordered, Robust, Three-Dimensional Gold Nanocrystal/Silica Arrays. *Science* **2004**, *304*, 567–571.
31. Wu, Z. N.; Li, Y.; Liu, J.; Lu, Z.; Zhang, H.; Yang, B. Colloidal Self-Assembly of Catalytic Copper Nanoclusters into Ultrathin Ribbons. *Angew. Chem., Int. Ed.* **2014**, *53*, 12196–12200.
32. Korösl, G.; Kováts, E. S. Density and Surface Tension of 83 Organic Liquids. *J. Chem. Eng. Data* **1981**, *26*, 323–332.
33. Li, Z.; Peng, X. Size/shape-Controlled Synthesis of Colloidal CdSe Quantum Disks: Ligand and Temperature Effects. *J. Am. Chem. Soc.* **2011**, *133*, 6578–6586.
34. Seo, J.; Jun, Y.; Park, S.; Nah, H.; Moon, T.; Park, B.; Kim, J.; Kim, Y.; Cheon, J. Two-Dimensional Nanosheet Crystals. *Angew. Chem., Int. Ed.* **2007**, *46*, 8828–8831.
35. Jang, J.; Jeong, S.; Seo, J.; Kim, M.; Sim, E.; Oh, Y.; Nam, S.; Park, B.; Cheon, J. Ultrathin Zirconium Disulfide Nanodiscs. *J. Am. Chem. Soc.* **2011**, *133*, 7636–7639.
36. Acharya, S.; Dutta, M.; Sarkar, S.; Basak, D.; Chakraborty, S.; Pradhan, N. Synthesis of Micrometer Length Indium Sulfide Nanosheets and Study of Their Dopant Induced Photoresponse Properties. *Chem. Mater.* **2012**, *24*, 1779–1785.
37. Nie, Z.; Park, J. I.; Li, W.; Bon, S. A. F.; Kumacheva, E. An "Inside-Out" Microfluidic Approach to Monodisperse Emulsions Stabilized by Solid Particles. *J. Am. Chem. Soc.* **2008**, *130*, 16508–16509.
38. Jette, E. R.; Foote, F. Precision Determination of Lattice Constants. *J. Chem. Phys.* **1935**, *3*, 605–616.
39. Bulusu, S.; Zeng, X. C. Structures and Relative Stability of Neutral Gold Clusters: Au n (n=15−19). *J. Chem. Phys.* **2006**, *125*, 154303.